Article

Electro-Optically Tunable Multifunctional Metasurfaces

Ghazaleh Kafaie Shirmanesh, Ruzan Sokhoyan, Pin Chieh Wu, and Harry A Atwater

ACS Nano, **Just Accepted Manuscript** • Publication Date (Web): 30 Apr 2020

Electro-Optically Tunable Multifunctional Metasurfaces

Ghazaleh Kafaie Shirmanesh,[†] Ruzan Sokhoyan,[†] Pin Chieh Wu, [†,‡] and Harry A. Atwater[†,ª,*]

[†] Thomas J. Watson Laboratory of Applied Physics and [ª] Kavli Nanoscience Institute, California Institute of Technology, Pasadena, California 91125, USA

[‡] Department of Photonics, National Cheng Kung University, Tainan 70101, Taiwan

[*]E-mail: haa@caltech.edu

Abstract: Shaping the flow of light at the nanoscale has been a grand challenge for nanophotonics over decades. It is now widely recognized that metasurfaces represent a chip-scale nanophotonics array technology capable of comprehensively controlling the wavefront of light *via* appropriately configuring subwavelength antenna elements. Here, we demonstrate a reconfigurable metasurface that is multifunctional, *i.e.*, notionally capable of providing diverse optical functions in the telecommunication wavelength regime, using a single compact, lightweight, electronically-controlled array with no moving parts. By electro-optical control of the phase of the scattered light from each identical individual metasurface element in an array, we demonstrate a single prototype multifunctional programmable metasurface that is capable of both dynamic beam steering and reconfigurable light focusing. Reconfigurable multifunctional metasurfaces with arrays of tunable optical antennas thus can perform arbitrary optical functions by programmable array-level control of scattered light phase, amplitude, and polarization, similar to dynamic and programmable memories in electronics.

Keywords: active metasurface, multifunctional, indium tin oxide, wavefront engineering, beam steering, focusing meta-mirror

Rapid advances in control of the phase and amplitude of the light scattered from planar arrays of nanophotonic elements has stimulated the development of metasurfaces that utilize amplitude/phase-sensitive scattering to enable wavefront engineering.[1, 2] Metasurfaces are also now demonstrating some of their potential applications in compact, high-performance, and low-cost optical devices and components, creating burgeoning interest in photonic integration. To date, metasurfaces have mostly been designed in an application-specific manner and the design process resulted in bespoke architectures tailored to particular applications. Dynamical control of the properties of the scattered light is possible by using tunable metasurfaces, for which external stimuli such as electrical biasing, optical pumping, heating, or elastic strain can give rise to changes in the dielectric function or physical dimensions of the metasurface elements,[3] thereby modulating the antenna phase and amplitude response. Among these mechanisms, electrical tuning has been proven to be a robust, energy-efficient and reversible scheme for tuning active metasurfaces.[4-16]

The ability of metasurfaces to spectrally, temporally, or spatially manipulate the wavefront of light with very high spatial resolution, is expected to accelerate miniaturization of optical devices and integration of optical systems.[17] However, in spite of advances in active metasurfaces to date, multifunctional reprogrammable metasurface components have not yet been demonstrated. Realization of a single hardware device that can provide multiple and --indeed general-- functions would further accelerate the impact of metasurfaces and their applications. Such multifunctionality can be found in electronics technology that has benefitted from development of programmable and reprogrammable circuits composed of identical circuit elements, such as dynamic[18] and static[19] random access memories and field-programmable gate arrays.[20] In this paper, we demonstrate a state-of-the-art prototypical multifunctional metasurface which can be electronically programmed to achieve two of the most essential functions identified to date for metasurfaces, namely, beam steering and focusing of light.

Optical beam steering is the key element of a broad range of optical systems such as light detection and ranging (LiDAR),[21] optical interconnects,[22] and optical communications.[23] Conventional beam steering devices such as Risley prisms,[24] galvanometer-scanning mirrors,[25] and decentered lenses[26] employ mechanically moving optical components to steer the incident light. Although mechanical beam steering systems provide wide steering angular range and large number of resolvable beam directions, they suffer from low steering speed due to the inertia of their moving parts and the weight of their mechanical components.[27] The availability of electronic beam steering arrays at near infrared (NIR) wavelengths with scanning frequencies above the MHz range could replace mechanical components with compact and lightweight optoelectronic alternatives and enable diverse functions unachievable *via* mechanical motion.

Reconfigurable metasurfaces have recently been employed to provide dynamic beam steering in the microwave and NIR regimes by exploiting microfluidic flows,[28, 29] incorporation of phase-change materials,[30] and reorientation of liquid crystals.[31] However, the performance of these devices is limited due to their failure to provide an exquisite control over the phase of the scattered light and accurately generate a desired phase profile, leaving them unable to demonstrate arbitrary functions. Alternatively, electro-optic modulation in multiple-quantum-well resonant metasurfaces,[32, 33] an intrinsically ultrafast process, has been shown to provide high-speed modulation and dynamic beam steering, but to date, a limited phase modulation range has constrained the achievable beam directivity and steering angle range.

Electro-optically controllable beam-switching has also been demonstrated *via* incorporation of transparent conducting oxides as active material into metasurfaces.[4, 34, 35] However, individual control over each metasurface element, which is required for more complex phase distribution patterns, has not been reported. Other researchers have demonstrated beam steering using waveguide-based thermo-optical phase shifters coupled to antennas[36-40] or by employing frequency-gradient metasurfaces.[41] These chip-based antenna arrays can enable beam steering at visible or infrared frequencies, but are application-specific, and hence, has been unable to achieve more general array functionalities.

Light focusing is another paramount optical function that plays a fundamental role in almost every optical system such as imaging, microscopy, optical data storage, and optical encryption.[42] Metasurfaces have given rise to versatile metalenses that can replace bulky conventional lenses by engineering the spatial variation of field amplitude or phase distribution over arrays of individual metasurface elements at approximately wavelength-scale or smaller spacing.[43-47] Metalenses have demonstrated the capability to

perform high-resolution imaging, wavefront shaping for aberration correction, and polarization conversion.[1, 2, 48]

Reconfigurable metasurfaces have been utilized to realize dynamic focusing by variation of the overall lens optical thickness or curvature, *via* liquid crystal reorientation,[49] microfluidic flow,[50, 51] or elastic deformation.[52] However, these modes of dynamic focusing do not permit precise tailoring of the lens focal properties by arbitrary phase control of the lens phase elements.

Here, we design and realize a multifunctional electro-optically tunable metasurface that can exhibit multiple functions in the NIR wavelength regime using a single device, *via* precise tailoring of the phase profile of an optical aperture. Figure 1a schematically illustrates this metasurface, whose independently addressable elements enable dynamic control of the wavefront *via* a pixel-by-pixel reconfiguration. Using this scheme, we demonstrate a reprogrammable metasurface whose function can be reconfigured between dynamic beam steering (Figure 1b) and dynamic focusing meta-mirrors, achieving a reconfigurable focal length and numerical aperture (Figure 1c) by tuning of the gate voltages applied to individual metasurface elements.

Results and Discussions

Design of Electro-Optically Tunable Metasurface Element

Figure 2a,b schematically illustrates the building blocks of our tunable gated field-effect metasurface, consisting of an Au back-reflector, on top of which an Al_2O_3 layer is deposited. The Al_2O_3 layer acts as a dielectric spacer, adding a degree of freedom for the metasurface optical mode profile design. This layer is followed by deposition of an indium-tin-oxide (ITO) layer, a gate dielectric, and Au 'fishbone' nanoantennas. The fishbone nanoantennas are comprised of patch antennas that are connected together by Au stripes, which also serve as gate voltage control electrodes. The gate dielectric is a hafnium/aluminum oxide nanolaminate (HAOL), a hybrid material that simultaneously exhibits high breakdown field and high DC permittivity[6] (see Supporting Information, Part 1 for a comparison between the proposed metasurface design and the dual-gated metasurface design[6]). We apply a DC electric bias between the ITO layer and the nanoantennas. This causes the ITO layer to undergo a reproducible field-effect-induced index change. By altering the applied electric field, one can modulate the ITO charge carrier density close to the interface of the ITO and the gate dielectric. By further increasing the applied bias, the real part of the dielectric permittivity in an accumulation layer located within ITO takes values between -1 and +1, yielding an epsilon-near-zero (ENZ) condition. In the ENZ regime, the ITO layer permittivity is varied at NIR wavelengths by changing the applied DC bias (see Supporting Information, Part 2).

The width and length of the antenna, and the width of the electrode are designed so that a magnetic dipole plasmon resonance occurs at the wavelengths coinciding with the ENZ regime for ITO, operating in the telecommunication wavelength regime. As a result of the spectral overlap of the ENZ regime of ITO and the geometrical resonance of the metasurface, the metasurface is expected to exhibit large phase modulation.

Optical Modulation in Electro-Optically Tunable Metasurface Element

Figure 2c shows the reflectance spectrum of the metasurface for different applied biases. As seen in Figure 2c, at all applied biases, resonant dips are clearly observed at wavelengths close to $\lambda = 1500$ nm, our wavelength of interest. Figure 2d,e illustrates the simulated reflectance and phase shift as a function of applied bias at different wavelengths. Here, phase shift is defined as a difference between the phases of the reflected and incident plane waves calculated at the same spatial point.

As can be seen, when the external bias is changed, we observe a reflectance change that is accompanied by significant phase modulation. This demonstrates that both the real and imaginary parts of the refractive index of the active region in the ITO layer are modulated by the applied bias. Once we obtained the reflectance and phase shift spectrum of the designed metasurface under applied bias, we can then pick the operation wavelength of the beam steering and focusing devices. To accomplish this, we utilize the

metasurface as a phase modulator, for which the reflectance should ideally remain constant upon change in the applied bias. Here the operation wavelength of λ = 1510 nm is chosen so that we obtain a phase shift of higher than 270° while the maximum reflectance modulation remains as small as possible (see Methods and Supporting Information, Part 3). After confirming this tunable response, we experimentally obtained the reflectance and phase shift of the fabricated metasurface under applied bias. Figure 2f illustrates the measured reflectance (blue curve) and phase shift (red curve) as a function of applied bias. In order to experimentally evaluate the reflection phase shift from the metasurface, we used a Michelson interferometer system.[6, 8] By focusing the incident laser beam on the edge of the metasurface nano-antenna array, the scattered beam is reflected partly from the metasurface and partly from the gold back-plane, resulting in a lateral shift in the interference fringe patterns of the metasurface and the back-reflector when changing the applied bias. By fitting these two cross sections to sinusoidal functions and obtaining the relative delay between the fitted sinusoidal curves when changing the applied voltage, we could retrieve the phase shift acquired due to the applied bias. As seen in Figure 2f, at an operation wavelength of λ=1522 nm, an actively tunable continuous phase shift of 0° to 274° is accompanied by a non-negligible reflectance modulation. When analyzing beam steering performance of our multifunctional metasurface, we observe that the mentioned reflectance modulation results in the increased intensity of the undesired side-lobes in the far-field radiation pattern (see Supporting Information, Part 12 for the effect of the reflectance modulation on the beam steering performance of our multifunctional metasurface). Moreover, since the complex dielectric permittivity of ITO is significantly modulated only in a sub-nm-thick layer, a large tunable phase shift is observed only when the optical field is tightly confined in this sub-nm-thick ITO active layer. This tight field confinement results in enhanced absorbance and, hence, reduced reflectance of our active metasurface. Changing the thickness of the dielectric Al_2O_3 and HAOL layers, or using transparent conducting oxides with higher electron mobilities, such as cadmium oxide (CdO),[53] one can increase the reflectance of the metasurface (see Supporting Information, Part 4).

Once we validated the modulation performance of the individual metasurface elements, we investigated the metasurface array beam steering and focusing performance. Scanning electron microscopy (SEM) images of the fabricated metasurface nanoantennas are shown in Figure 3a. In our metasurface device, nanoantennas are electrically bus-connected together in one direction, forming equipotential antenna rows, referred to here as a metasurface pixel. Then each pixel is individually controlled by a separate applied gate voltage. Figure 3b is a photomicrograph of the fabricated array, consisting of 96 individually-controllable and identical metasurface pixels (see Methods and Supporting Information, Part 5 for fabrication steps). In order to individually bias each of these metasurface pixels, we designed two printed circuit boards (PCBs). Figure 3c shows the first PCB with the multifunctional metasurface mounted on and wire-bonded to it. Each conducting pad on the first PCB is then connected to an external pin on the second PCB that is shown in Figure 3d. This voltage deriving PCB is capable of providing 100 independent voltages that can be individually controlled through programming a number of micro-controllers by a computer (see Methods).

In order to characterize our multifunctional metasurface, we used a custom-built optical setup to measure reflectance spectrum, phase shift, beam steering profile, and focused beam profile (see Supporting Information, Part 6-10 for a detailed description of the measurements).

Demonstration of Beam Steering

After validating the wide phase tunability of our metasurface, we designed and demonstrated a dynamic beam steering device. In order to implement beam steering, we designed the spatial phase profile of the light reflected from the metasurface by engineering the spatial distribution of the DC bias voltages applied to the 96 metasurface pixels (see Supporting Information, Part 11).

In order to design the spatial phase profile of the metasurface, we employed a multilevel approximation of blazed grating approach[54-56] that is widely used for demonstration of beam steering metasurfaces.[31, 32, 34] Here, we discretized the phase shift acquired by the metasurface pixels into four levels 0°, 90°, 180°, and 270° (see Supporting Information, Part 12 for a discussion on the choice of phase distribution). In this

configuration, the metasurface acts as a diffraction grating with reconfigurable periodicity. Each effective period, hereafter termed a supercell, consists of the metasurface pixels exhibiting the discretized 4-level phase shift values. When no bias is applied, we observed only the zeroth order diffracted beam in the Fourier plane. In other words, the subwavelength period of the metasurface results in an absence of higher-order diffracted beams at zero bias. By changing the pixel repetition number (*RN*) for each phase shift value within one supercell, we electrically modulated the effective periodicity of the metasurface array. This resulted in a shift of the spatial position of the first diffracted order, enabling manipulation of the far-field radiation.

Figure 4a shows the metasurface spatial phase profiles, for the four-level phase shift with different *RN* values. In Figure 4a, each gray-shaded region determines one supercell in each case. The simulated far-field pattern of the beam steering device is presented in Figure 4b (see Supporting Information, Part 12 for simulation methods). It should be noted that the simulations correspond to the dimensions of our fabricated metasurface that showed an average pitch size of 504 nm. As can be seen, by changing the *RN* value, the size of the metasurface supercell is electrically modulated, resulting in reconfigurable beam steering with quasi-continuous steering angles that can be as large as ~70.5° for our metasurface design with a pitch size of 400 nm (see Supporting Information, Part 12). Figure 4c shows the measured far-field pattern for our beam steering device. Due to limitations of our measurement setup, steering angles of higher than 23.5° could not be captured by the imaging system. As a result, the maximum measured steering angle was ~22°, which corresponds to a repeat number of 2. As expected, by increasing the effective period of the metasurface, the beam angle becomes smaller. We also note that for each *RN* value, no diffracted order with an intensity equal to that of the desired steering angle is observed at negative angles, indicating true phase gradient beam steering rather than switchable diffraction. This confirms that the beam steering is obtained as a result of the asymmetric phase gradient introduced by the subwavelength metasurface phase elements.

Demonstration of Dynamic Focusing Meta-Mirror

Using the same concept of controlling the phase imposed by each individual metasurface pixel, we were able to demonstrate use of our multifunctional metasurface as a reconfigurable lens by developing phase profiles for lenses with different focal lengths. Figure 5a-c shows the spatial distribution of the phase shift (diamond) and the corresponding applied bias voltage (square) required to focus the reflected beam at focal lengths of 1.5 μm, 2 μm and 3 μm. These values were extracted from the simulated phase shift as a function of applied bias (see Supporting Information, Part 13). In order to investigate the focusing performance, we simulated the multifunctional metasurface under the applied bias distributions illustrated in Figure 5a-c. In our full-wave electromagnetic simulations, we modeled a miniaturized lens with a 20 μm aperture size since simulating the full metasurface at the small mesh sizes required for the ITO layer active region is beyond our present numerical simulation capability. Figure 5d-f illustrate the far-field pattern of the beam reflected from our tunable metasurface in the x-z plane. As seen in Figure 5d-f, the metasurface can clearly focus the reflected light at the focal lengths of 1.5 μm, 2 μm and 3 μm, when appropriate bias voltages are applied to the individual metasurface pixels.

We then experimentally characterized the dynamic focusing meta-mirror once the focusing performance of our multifunctional metasurface was confirmed by calculations. We programmed the voltages applied to each metasurface pixel in order to experimentally achieve the desired phase shift values (Figure 2f) (see Supporting Information, Part 13). Then the fabricated focusing meta-mirror was characterized utilizing our multifunctional setup (see Supporting Information, Part 10). Using this setup, the intensity profile of the reflected beam in the *xy*-plane was recorded. By extracting the cross sections of the captured intensity profiles at fixed *y* values, we reconstructed the intensity profile of the reflected beam in the *xz*-plane. Figure 5g-i illustrate the metasurface reflected beam intensity profiles in the *xz*-plane for the applied bias distributions shown in Figure 5a-c. As can be seen, the fabricated metasurface focuses the reflected beam at the desired depths. The scale bars in Figure 5g-i were obtained by imaging an object of known size. When the incident light was polarized perpendicular to the antennas, no focusing was observed

since no phase modulation could be achieved in that polarization. This observation confirmed that the captured focusing originated from the metasurface.

Using the same concept of individually-controlled metasurface pixels, we reprogrammed the applied bias voltages to the metasurface in order to experimentally demonstrate a tunable focusing meta-mirrors with focal length varying from 15 μm to 25 μm (see Supporting Information, Part 14).

Conclusions

We have designed and experimentally demonstrated an electrically tunable multifunctional metasurface in the NIR wavelength range. The multifunctional metasurface is realized *via* field-effect-induced modulation of transparent conducting oxide active regions incorporated into the metasurface and is capable of spatiotemporal modulation of the fundamental attributes of light. As a proof of concept, we designed phase profiles for our multifunctional metasurface to demonstrate beam steering and dynamic focusing using the same device *via* individually controlling each metasurface pixel. Such a multifunctional metasurface can initiate integrated on-chip electro-optical devices such as light detection and ranging (LiDAR) systems. Prior research has shown that the reflectance of the ITO-based active metasurfaces can be considerably enhanced by utilizing ITO-integrated all-dielectric guided-mode resonance mirror designs.[57] The efficiency of the multifunctional metasurface can possibly be further improved *via* optimization algorithms.[58-61] It has been previously shown that optimization algorithms may yield non-trivial structural shapes and metasurface antenna distributions that yield significantly improved optical performance. In particular, optimization algorithms may significantly boost the performance of active beam steering metasurfaces.[62] A worthy direction for future research is to extend the multifunctional metasurface concept demonstrated here to a two-dimensional phased array architecture. In addition to enabling beam steering and focusing in two dimensions, such a two-dimensional array could enable fast and energy-efficient programmable devices such as dynamic holograms, off-axis lenses, axicons, vortex plates, and polarimeters.

Methods

Full-wave simulation of reconfigurable metasurface

Full full-wave electromagnetic calculations for our tunable metasurface were performed using finite difference time domain optical simulations (FDTD Lumerical). Figure S3a shows the calculated phase shift spectrum at different applied biases.

After we confirmed that our designed metasurface can provide both reflectance (Figure 3a-c of main manuscript) and phase (Figure S3a) modulation, we chose the operating wavelength of the device such that the metasurface could provide a large phase modulation and as modest reflectance modulation as possible. Figure S3b shows the maximum reflectance modulation and the maximum achievable phase shift at different wavelengths. As can be seen, at $\lambda = 1510$ nm, a phase shift larger than 270° is achievable while the reflectance change is kept to be as modest as possible.

Multifunctional metasurface fabrication

The metasurface fabrication steps are illustrated in Figure S8. In order to fabricate the multifunctional metasurface device, we first did a standard cleaning process on Si wafers. Then we patterned the outmost part of the connecting pads as well as some alignment markers using photolithography. After developing the photoresist, a 10 nm-thick Ti layer followed by 200 nm-thick Au layer was deposited on the samples using electron beam evaporator. After lifting-off the excess Ti-Au parts, we patterned the back reflector by electron beam lithography [VISTEC electron beam pattern generator (EBPG) 5000+] at an acceleration voltage of 100 keV. After developing the electron beam resist, we deposited a 3 nm-thick Cr layer followed by 80 nm-thick Au layer using electron beam evaporator. After the lift-off process, a 9.5 nm-thick Al_2O_3

layer was deposited on the samples using atomic layer deposition (ALD) through shadow masks. After developing the electron beam resist, the ITO layer was patterned by electron beam lithography, and a 5 nm-thick ITO layer was deposited on the sample using room-temperature RF magnetron sputtering in Ar/O_2 plasma environment. The deposition pressure is 3 mTorr while the applied RF power is 48W. Once the excess ITO regions were lifted off, we patterned the contact pads of the ITO layer by electron beam lithography. A 10 nm-thick Ti layer followed by 200 nm-thick Au layer was then deposited on the samples using electron beam evaporator after developing the electron beam resist. Afterwards, a 9.5 nm-thick HAOL layer was deposited on the samples using ALD. The size of the HAOL film was controlled by using shadow masks during the atomic layer deposition. Then we patterned the antennas by electron beam lithography and made the inner contact pad connections. Once the electron beam resist was developed, we deposited a 1.5 nm-thick Ge layer followed by a 40 nm-thick Au layer.

Electrical connections to individually control metasurface pixels

In order to individually bias each of 96 different metasurface elements, we designed two printed circuit boards (PCBs). The sample is mounted on the first PCB (P_1), and 96 individual metasurface elements as well as 4 ITO connecting pads (to be used as the ground) are wire-bonded to 100 conducting pads on the PCB (Figure 3c of main manuscript). Each conducting pad on P_1 is then connected to an external pin on the second PCB (P_2). This voltage deriving PCB is capable of providing 100 independent voltages that can be individually controlled (Figure 3d of main manuscript). These independent bias voltages are produced by programming 12 digital to analog converters (DACs). Every set of three DACs is programmed by an Arduino Nano micro-controller board based on the ATmega328P (Arduino Nano 3.x). In order to provide the desired voltages at the output ports of the DACs, the input ports of the DACs are connected to the digital outputs of the Arduino microcontrollers and are then programmed *via* computer by using the Arduino Software (IDE).

ASSOCIATED CONTENT

Supporting Information

The Supporting Information is available free of charge at:

> Comparison to the previously proposed design; Calculating electrostatic properties of ITO; Full-wave simulation of reconfigurable metasurface; Increasing metasurface reflectance level; Multifunctional metasurface fabrication; Universal measurements setup; Reflectance measurements; Phase shift measurements; Beam steering measurements; Reconfigurable focusing measurements; Choosing the number of metasurface pixels; Beam steering metasurface simulations; Spatial phase and voltage profiles for reconfigurable focusing meta-mirror; Reconfigurable focusing meta-mirror: accessing longer focal lengths.

Pre-print version is available at: Kafaie Shirmanesh, G.; Sokhoyan, R.; Wu, P. C.; Atwater, H. A., Electro-Optically Tunable Universal Metasurfaces. 2019, 1910.02069. arXiv: physics.optics. http://arxiv.org/abs/1910.02069 (Accessed Oct 4, 2019)

AUTHOR INFORMATION

ORCID

Ghazaleh Kafaie Shirmanesh: 0000-0003-1666-3215.

Ruzan Sokhoyan: 0000-0003-4599-6350.

Pin Chieh Wu: 0000-0002-5781-9696.

Harry A. Atwater: 0000-0001-9435-0201.

Author Contributions

G.K.S, R.S., and H.A.A conceived the original idea. G.K.S performed the numerical design, device fabrication, performed the optical measurements, analyzed numerical and experimental data, designed and build up the PCB for individually electrical control of metasurface elements, helped with the build-up of optical setup for measurement, and wrote the manuscript. P.C.W built up the optical setup, performed the numerical simulations for beam steering and focusing. R.S. performed the device physics numerical calculations, helped with data analysis, and wrote the manuscript. H.A.A. organized the project, designed experiments, analyzed the results, and prepare the manuscripts. All authors discussed the results and commented on the manuscript.

The authors declare no competing financial interest.

ACKNOWLEDGEMENTS

The authors acknowledge metasurface device fabrication support provided by the Kavli Nanoscience Institute (KNI).

Funding: This work was supported by Samsung Electronics and the National Aeronautics and Space Administration. P.C.W. acknowledges the support from Ministry of Science and Technology, Taiwan (Grant number: 107-2923-M-006-004-MY3; 108-2112-M-006-021-MY3). P.C.W. also acknowledges the support in part by Higher Education Sprout Project, Ministry of Education to the Headquarters of University Advancement at National Cheng Kung University (NCKU).

Reference

1. Hsiao, H. H.; Chu, C. H.; Tsai, D. P., Fundamentals and Applications of Metasurfaces. *Small Methods* **2017,** *1*, 1600064.
2. Kildishev, A. V.; Boltasseva, A.; Shalaev, V. M., Planar Photonics with Metasurfaces. *Science* **2013,** *339*, 1232009.
3. Shaltout, A. M.; Shalaev, V. M.; Brongersma, M. L., Spatiotemporal Light Control with Active Metasurfaces. *Science* **2019,** *364*, eaat3100.
4. Huang, Y.-W.; Lee, H. W. H.; Sokhoyan, R.; Pala, R. A.; Thyagarajan, K.; Han, S.; Tsai, D. P.; Atwater, H. A., Gate-Tunable Conducting Oxide Metasurfaces. *Nano Lett.* **2016,** *16*, 5319-5325.
5. Sherrott, M. C.; Hon, P. W.; Fountaine, K. T.; Garcia, J. C.; Ponti, S. M.; Brar, V. W.; Sweatlock, L. A.; Atwater, H. A., Experimental Demonstration of > 230 Phase Modulation in Gate-Tunable Graphene–Gold Reconfigurable Mid-Infrared Metasurfaces. *Nano Lett.* **2017,** *17*, 3027-3034.
6. Shirmanesh, G. K.; Sokhoyan, R.; Pala, R. A.; Atwater, H. A., Dual-Gated Active Metasurface at 1550 nm with Wide (>300°) Phase Tunability. *Nano Lett.* **2018,** *18*, 2957–2963.
7. Thyagarajan, K.; Sokhoyan, R.; Zornberg, L.; Atwater, H. A., Millivolt Modulation of Plasmonic Metasurface Optical Response *via* Ionic Conductance. *Adv. Mater.* **2017,** *29*, 1701044.
8. Kim, Y.; Wu, P. C.; Sokhoyan, R.; Mauser, K.; Glaudell, R.; Shirmanesh, G. K.; Atwater, H. A., Phase Modulation with Electrically Tunable Vanadium Dioxide Phase-Change Metasurfaces. *Nano Lett.* **2019,** *19*, 3961-3968.
9. Jun, Y. C.; Reno, J.; Ribaudo, T.; Shaner, E.; Greffet, J.-J.; Vassant, S.; Marquier, F.; Sinclair, M.; Brener, I., Epsilon-Near-Zero Strong Coupling in Metamaterial-Semiconductor Hybrid Structures. *Nano Lett.* **2013,** *13*, 5391-5396.

10. Forouzmand, A.; Salary, M. M.; Shirmanesh, G. K.; Sokhoyan, R.; Atwater, H. A.; Mosallaei, H., Tunable All-Dielectric Metasurface for Phase Modulation of the Reflected and Transmitted Light *via* Permittivity Tuning of Indium Tin Oxide. *Nanophotonics* **2019,** *8*, 415-427.
11. Park, J.; Kang, J. H.; Kim, S.; Liu, X. G.; Brongersma, M. L., Dynamic Reflection Phase and Polarization Control in Metasurfaces. *Nano Lett.* **2017,** *17*, 407–413.
12. Zhu, Z.; Evans, P. G.; Richard, O.; Haglund, F.; Valentine, J. G., Dynamically Reconfigurable Metadevice Employing Nanostructured Phase-Change Materials. *Nano Lett.* **2017,** *17*, 4881-4885.
13. Iyer, P. P.; Pendharkar, M.; Schuller, J. A., Electrically Reconfigurable Metasurfaces Using Heterojunction Resonators. *Adv. Opt. Mater.* **2016,** *4*, 1582-1588.
14. Decker, M.; Kremers, C.; Minovich, A.; Staude, I.; Miroshnichenko, A. E.; Chigrin, D.; Neshev, D. N.; Jagadish, C.; Kivshar, Y. S., Electro-Optical Switching by Liquid-Crystal Controlled Metasurfaces. *Opt. Express* **2013,** *21*, 8879–8885.
15. Komar, A.; Fang, Z.; Bohn, J.; Sautter, J.; Decker, M.; Miroshnichenko, A.; Pertsch, T.; Brener, I.; Kivshar, Y. S.; Staude, I.; Neshev, D. N., Electrically Tunable All-Dielectric Optical Metasurfaces Based on Liquid Crystals. *Appl. Phys. Lett.* **2017,** *110*, 071109.
16. Sautter, J.; Staude, I.; Decker, M.; Rusak, E.; Neshev, D. N.; Brener, I.; Kivshar, Y. S., Active Tuning of All-Dielectric Metasurfaces. *ACS Nano* **2015,** *9*, 4308-4315.
17. Yu, N.; Genevet, P.; Kats, M. A.; Aieta, F.; Tetienne, J.-P.; Capasso, F.; Gaburro, Z., Light Propagation with Phase Discontinuities: Generalized Laws of Reflection and Refraction. *Science* **2011,** *334*, 333–337.
18. Adams, R. D., Dynamic Random Access Memories. In *High Performance Memory Testing: Design Principles, Fault Modeling and Self-Test*, Springer US: Boston, MA, 2003; pp 77-87.
19. Adams, R. D., Static Random Access Memories. In *High Performance Memory Testing: Design Principles, Fault Modeling and Self-Test*, Springer US: Boston, MA, 2003; pp 17-46.
20. Brown, S. D.; Francis, J. R.; Rose, J.; Vranesic, Z. G., Introduction to FPGAs. In *Field-Programmable Gate Arrays*, Springer US: Boston, MA, 1992; pp 1-11.
21. Schwarz, B., Mapping the World in 3D. *Nat. Photonics* **2010,** *4*, 429–430.
22. Chaintoutis, C.; Shariati, B.; Bogris, A.; Dijk, P. V.; Roeloffzen, C. G. H.; Bourderionnet, J.; Tomkos, I.; Syvridis, D., Free Space Intra-Datacenter Interconnects Based on 2D Optical Beam Steering Enabled by Photonicintegrated Circuits. *Photonics Res.* **2018,** *5*, 21.
23. Feng, F.; White, I. H.; Wilkinson, T. D., Free Space Communications with Beam Steering a Two-Electrode Tapered Laser Diode Using Liquid-Crystal SLM. *J. Lightwave Technol.* **2013,** *31*, 2001.
24. Duncan, B. D.; Bos, P. J.; Sergan, V., Wide-Angle Achromatic Prism Beam Steering for Infrared Countermeasure Applications. *Opt. Eng.* **2003,** *42*, 1038–1047.
25. Jofre, M.; Anzolin, G.; Steinlechner, F.; Oliverio, N.; Torres, J. P.; Pruneri, V.; Mitchell, M. W., Fast Beam Steering with Full Polarization Control Using a Galvanometric Optical Scanner and Polarization Controller. *Opt. Express* **2012,** *20*, 12247.
26. Gibson, J. L.; Duncan, B. D.; Watson, E. A.; Loomis, J. S., Wide-Angle Decentered Lens Beam Steering for Infrared Countermeasures Applications. *Opt. Eng.* **2004,** *43*, 2312.
27. Oh, C. W. Free-Space Transmission with Passive Two-Dimensional Beam Steering for Indoor Optical Wireless Networks. Technische Universiteit Eindhoven, Eindhoven, 2017.
28. Naqvi, A. H.; Lim, S., A Beam-Steering Antenna with a Fluidically Programmable Metasurface. *IEEE Trans. Antennas Propag.* **2019,** *67*, 3704-3711.
29. Chen, L.; Ruan, Y.; Cui, H. Y., Liquid Metal Metasurface for Flexible Beam-Steering. *Opt. Express* **2019,** *27*, 23282-23292.
30. Galarreta, C. R. d.; Alexeev, A. M.; Au, Y. Y.; Lopez-Garcia, M.; Klemm, M.; Cryan, M.; Bertolotti, J.; Wright, C. D., Nonvolatile Reconfigurable Phase-Change Metadevices for Beam Steering in the Near Infrared. *Adv. Funct. Mater.* **2018,** *28*, 1704993.
31. Li, S.-Q.; Xu, X.; Veetil, R. M.; Valuckas, V.; Paniagua-Domínguez, R.; Kuznetsov, A. I., Phase-Only Transmissive Spatial Light Modulator Based on Tunable Dielectric Metasurface. *Science* **2019,** *364*, 1087-1090.

32. Wu, P. C.; Pala, R. A.; Shirmanesh, G. K.; Cheng, W.-H.; Sokhoyan, R.; Grajower, M.; Alam, M. Z.; Lee, D.; Atwater, H. A., Dynamic Beam Steering with All-Dielectric Electro-Optic III-V Multiple-Quantum-Well Metasurfaces. *Nat. Commun.* **2019,** *10,* 3654.
33. Iyer, P. P.; Pendharkar, M.; Palmstrøm, C. J.; Schuller, J. A., III–V Heterojunction Platform for Electrically Reconfigurable Dielectric Metasurfaces. *ACS Photonics* **2019,** *6*, 1345-1350.
34. Howes, A.; Wang, W.; Kravchenko, I.; Valentine, J., Dynamic Transmission Control Based on All-Dielectric Huygens Metasurfaces. *Optica* **2018,** *5*, 787–792.
35. Sorger, V.; Lanzillotti-Kimura, N. D.; Ma, R.; Zhang, X., Ultra-Compact Silicon Nanophotonic Modulator with Broadband Response. *Nanophotonics* **2012,** *1*, 17-22.
36. DeRose, C. T.; Kekatpure, R. D.; Trotter, D. C.; Starbuck, A.; Wendt, J. R.; Yaacobi, A.; Watts, M. R.; Chettiar, U.; Engheta, N.; Davids, P. S., Electronically Controlled Optical Beam-Steering by an Active Phased Array of Metallic Nanoantennas. *Opt. Express* **2013,** *21*, 5198-5208.
37. Doylend, J. K.; Heck, M. J. R.; Bovington, J. T.; Peters, J. D.; Coldren, L. A.; Bowers, J. E., Two-Dimensional Free-Space Beam Steering with an Optical Phased Array on Silicon-on Insulator. *Opt. Express* **2011,** *19*, 21595-21604.
38. López, J. J.; Skirlo, S. A.; Kharas, D.; Sloan, J.; Herd, J.; Juodawlkis, P.; Soljačić, M.; Sorace-Agaskar, C. *Planar-Lens Enabled Beam Steering for Chip-Scale Lidar*. In Conference on Lasers and Electro-Optics, San Jose, CA, May 13-18, 2018; Optical Society of America; IEEE: 2018; SM3I.1.
39. Fatemi, R.; Abiri, B.; Khachaturian, A.; Hajimiri, A., High Sensitivity Active Flat Optics Optical Phasedarray Receiver with a Two-Dimensional Aperture. *Opt. Express* **2018,** *26*, 29983-29999.
40. Sun, J.; Timurdogan, E.; Yaacobi, A.; Hosseini, E. S.; Watts, M. R., Large-Scale Nanophotonic Phased Array. *Nature* **2013,** *493*, 195–199.
41. Shaltout, A. M.; Lagoudakis, K. G.; Groep, J. v. d.; Kim, S. J.; Vučković, J.; Shalaev, V. M.; Brongersma, M. L., Spatiotemporal Light Control with Frequency-Gradient Metasurfaces. *Science* **2019,** *365*, 374-377.
42. Tseng, M. L.; Hsiao, H.-H.; Chu, C. H.; Chen, M. K.; Sun, G.; Liu, A.-Q.; Tsai, D. P., Metalenses: Advances and Applications. *Adv. Opt.Mater.* **2018,** *6*, 1800554.
43. Chen, X. Z.; Huang, L. L.; Mühlenbernd, H.; Li, G. X.; Bai, B. F.; Tan, Q.; Jin, G.; Qiu, C. W.; Zhang, S.; Zentgraf, T., Dual-Polarity Plasmonic Metalens for Visible Light. *Nat. Commun* **2012,** *3*, 1198.
44. Khorasaninejad, M.; Shi, Z.; Zhu, A. Y.; Chen, W. T.; Sanjeev, V.; Zaidi, A.; Capasso, F., Achromatic Metalens over 60 nm Bandwidth in the Visible and Metalens with Reverse Chromatic Dispersion. *Nano Lett.* **2017,** *17*, 1819–1824.
45. Arbabi, A.; Horie, Y.; Bagheri, M.; Faraon, A., Dielectric Metasurfaces for Complete Control of Phase and Polarization with Subwavelength Spatial Resolution and High Transmission. *Nat. Nanotechnol.* **2015,** *10*, 937–943.
46. Liu, C.-H.; Zheng, J.; Colburn, S.; Fryett, T. K.; Chen, Y.; Xu, X.; Majumdar, A., Ultrathin van der Waals Metalenses. *Nano Lett.* **2018,** *18*, 6961-6966.
47. Colburn, S.; Zhan, A.; Majumdar, A., Varifocal Zoom Imaging with Large Area Focal Length Adjustable Metalenses. *Optica* **2018,** *5*, 825-831.
48. Yu, N. F.; Capasso, F., Flat Optics with Designer Metasurfaces. *Nat. Mater* **2014,** *13*, 139–150.
49. Lin, H. C.; Chen, M. S.; Lin, Y. H., A Review of Electrically Tunable Focusing Liquid Crystal Lenses. *Trans. Electr. Electron Mater.* **2011,** *12*, 234–240.
50. Chronis, N.; Liu, G. L.; Jeong, K. H.; Lee, L. P., Tunable Liquid-Filled Microlens Array Integrated with Microfuidic Network. *Opt. Express* **2003,** *11*, 2370–2378.
51. Zhu, W.; Song, Q.; Yan, L.; Zhang, W.; Wu, P.-C.; Chin, L. K.; Cai, H.; Tsai, D. P.; Shen, Z. X.; Deng, T. W.; Ting, S. K.; Gu, Y.; Lo, G. Q.; Kwong, D. L.; Yang, Z. C.; Huang, R.; Liu, A.-Q.; Zheludev, N., A Flat Lens with Tunable Phase Gradient by Using Random Access Reconfigurable Metamaterial. *Adv. Mater.* **2015,** *27*, 4739-4743.
52. Ee, H. S.; Agarwal, R., Tunable Metasurface and Flat Optical Zoom Lens on a Stretchable Substrate. *Nano. Lett.* **2016,** *16*, 2818–2823.

53. Yang, Y.; Kelley, K.; Sachet, E.; Campione, S.; Luk, T. S.; Maria, J.-P.; Sinclair, M. B.; Brener, I., Femtosecond Optical Polarization Switching Using a Cadmium Oxide-Based Perfect Absorber. *Nat. Photonics* **2017,** *11*, 390–395.
54. Gongjian, Z.; Man, Z.; Yang, Z., Wave Front Control with SLM and Simulation of Light Wave Diffraction. *Opt. Express* **2018,** *26*, 33543-33564.
55. Swanson, G. J. *Binary Optics Technology: The Theory and Design of Multi-Level Diffractive Optical Elements*; Technical Report 854, Massachusetts Institute of Technology: Cambridge, MA, 1989.
56. Swanson, G. J. *Binary Optics Technology: Theoretical Limits on the Diffraction Efficiency of Multilevel Diffractive Optical Elements*; Technical Report 914; Massachusetts Institute of Technology: Cambridge, MA, 1991.
57. Forouzmandand, A.; Mosallaei, H., Electro-Optical Amplitude and Phase Modulators Based on Tunable Guided-Mode Resonance Effect. *ACS Photonics* **2019,** *6*, 2860-2869.
58. Phan, T.; Sell, D.; Wang, E. W.; Doshay, S.; Edee, K.; Yang, J.; Fan, J. A., High-Efficiency, Large-Area, Topology-Optimized Metasurfaces. *Light Sci. Appl.* **2019,** *8*.
59. Campbell, S. D.; Sell, D.; Jenkins, R. P.; Whiting, E. B.; Fan, J. A.; Werner, D. H., Review of Numerical Optimization Techniques for Meta-Device Design. *Opt. Mater. Express,* **2019,** *9*, 1842-1863.
60. Liu, D.; Tan, Y.; Khoram, E.; Yu, Z., Training Deep Neural Networks for the Inverse Design of Nanophotonic Structures. *ACS Photonics* **2018,** *5*, 1365−1369.
61. Jafar-Zanjani, S.; Inampudi, S.; Mosallaei, H., Adaptive Genetic Algorithm for Optical Metasurfaces Design. *Sci. Rep.* **2018,** *8*, 11040.
62. Chung, H.; Miller, O. D., Tunable Metasurface Inverse Design for 80% Switching Efficiencies and 144° Angular Steering. 2019, 1910.03132. arXiv:physics.optics. https://arxiv.org/abs/1910.03132 (Accessed Oct 7, 2019).
63. C. A. Balanis, Fundamental Parameters and Figures-of-Merit of Antennas. In *Antenna Theory: Analysis and Design*, Edition 3, John Wiley & Sons: New York, 1997. Chapter 2, pp 44-57.
64. Engstrom, D.; Bengtsson, J.; Eriksson, E.; Goksor, M, Improved Beam Steering Accuracy of a Single Beam with a 1D Phase-Only Spatial Light Modulator. *Op. Express* **2008**, 16, 18275-18287.
65. Han, S.; Kim, S.; Kim, S.; Low, T.; Brar, V. W.; Jang, M. S., Complete Complex Amplitude Modulation with Electronically Tunable Graphene Plasmonic Metamolecules. *ACS Nano* **2020**, 14, 1166-1175.
66. Lin, R. J.; Su, V.-C.; Wang, S.; Chen, M. K.; Chung, T. L.; Chen, Y. H.; Kuo, H. Y.; Chen, J.-W.; Chen, J.; Huang, Y.-T.; Wang, J.-H.; Chu, C. H.; Wu, P. C.; Li, T.; Wang, Z.; Zhu, S.; Tsai, D. P., Achromatic Metalens Array for Full-Colour Light-Field Imaging. *Nat. Nanotechnol.* **2019**, 14, 227–231.
67. Wang, S.; Wu, P. C.; Su, V.-C.; Lai, Y.-C.; Chen, M.-K.; Kuo, H. Y.; Chen, B. H.; Chen, Y. H.; Huang, T.-T.; Wang, J.-H.; Lin, R.-M.; Kuan, C.-H.; Li, T.; Wang, Z.; Zhu, S.; Tsai, D. P., A Broadband Achromatic Metalens in the Visible. *Nat. Nanotechnol.* **2018**, 13, 227–232.

FIGURES

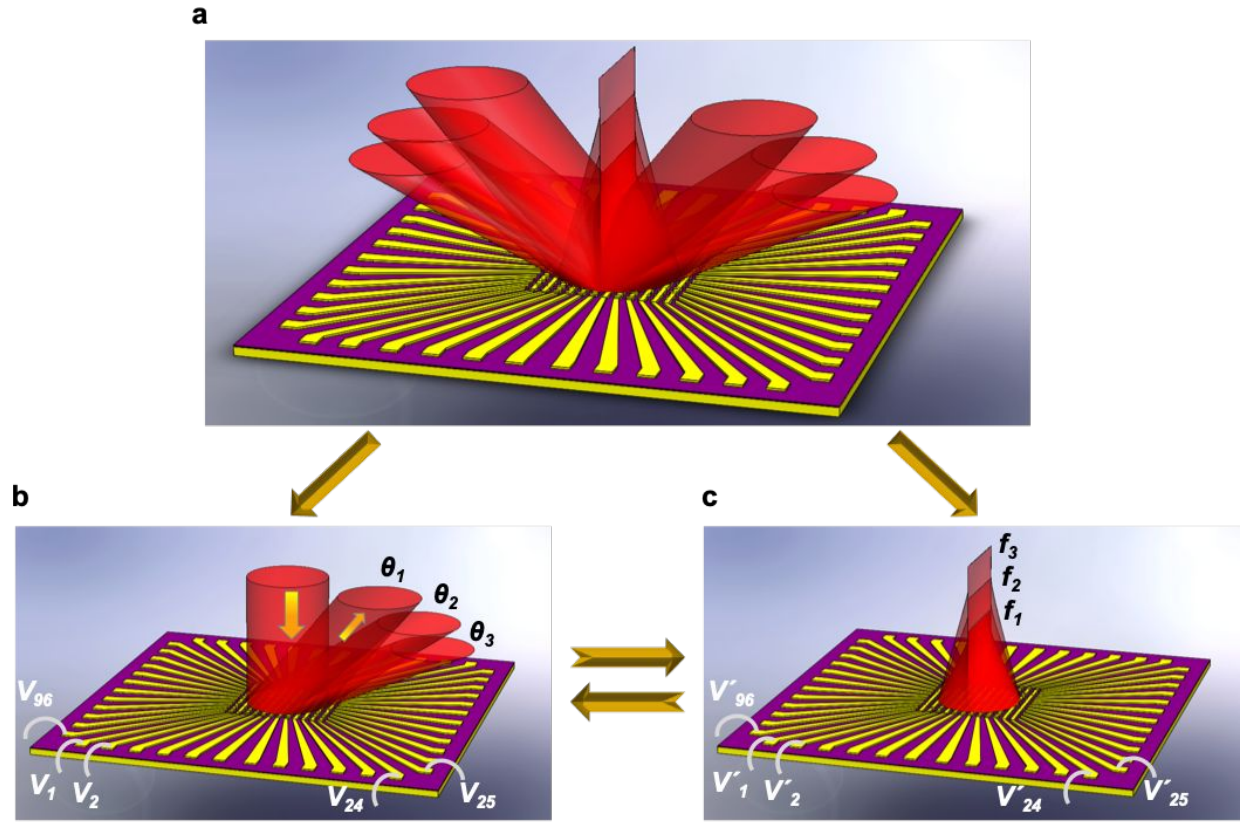

Figure 1. Multifunctional metasurface with 96 independently addressable metasurface elements. Schematic of (a) the multifunctional metasurface whose functionality can be switched between (b) dynamic beam steering and (c) cylindrical metalens with reconfigurable focal length.

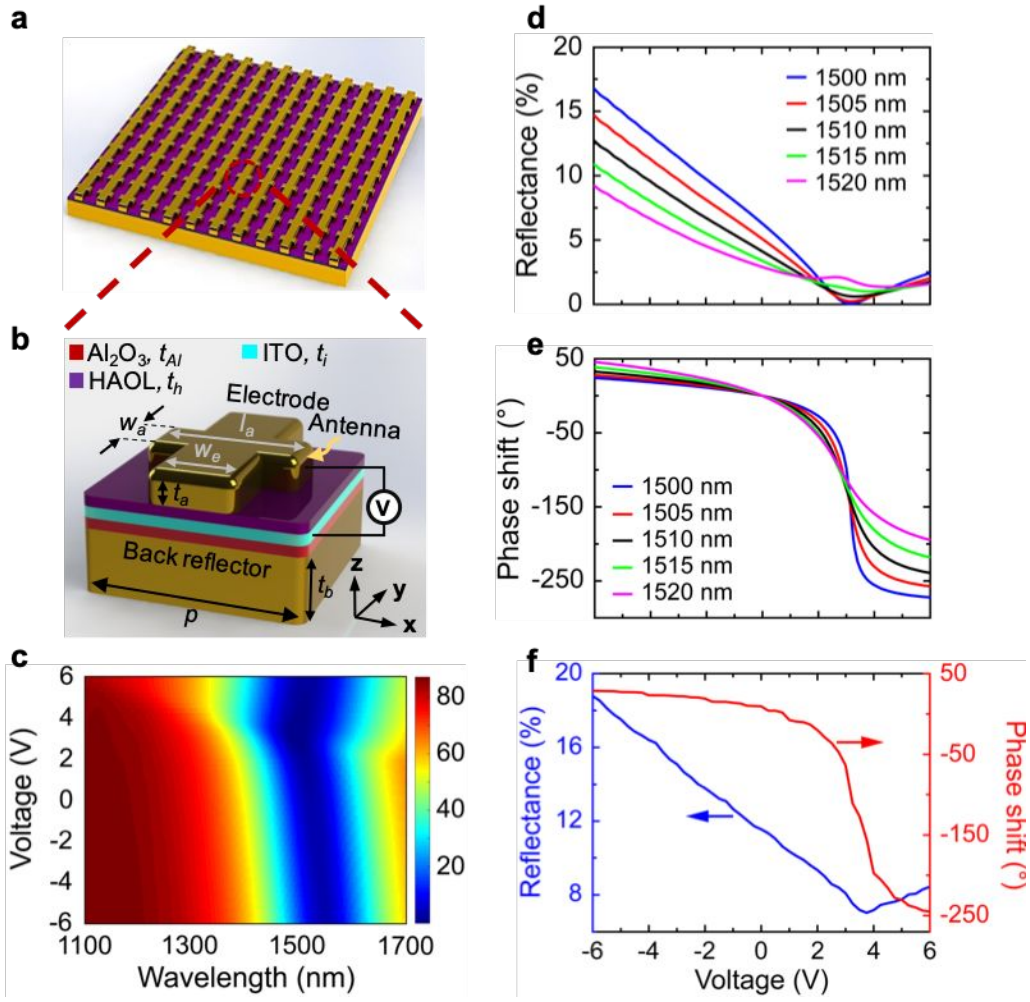

Figure 2. Unit cell design of the multifunctional metasurface. Schematic of (a) periodic array and (b) unit cell of the antenna elements. The metasurface is composed of an Au back-reflector, an Al_2O_3 dielectric layer, an ITO layer, and a hafnium oxide/aluminum oxide laminated (HAOL) gate dielectric followed by an Au fishbone antenna. The periodicity of the metasurface is p = 400 nm, and the thickness of the back-reflector, Al_2O_3, ITO, and HAOL layers are t_b = 80 nm, t_{Al} = 9.5 nm, t_i = 5 nm, and t_h = 9.5 nm, respectively. The width, length, and the thickness of the antenna are w_a=130 nm, l_a = 230 nm, and t_a = 40 nm, respectively and the width of the electrode is w_e = 150 nm. (c) Simulated reflectance spectrum at different bias voltages. Simulated (d) reflectance and (e) phase of the reflection from the metasurface as a function of applied voltage for different wavelengths. (f) Measured reflectance (blue curve) and phase shift (red curve) as a function of applied bias voltage. The operation wavelength of the fabricated device was chosen to be λ = 1522 nm such that a phase shift greater than 270° accompanied by moderate amplitude variation could be obtained.

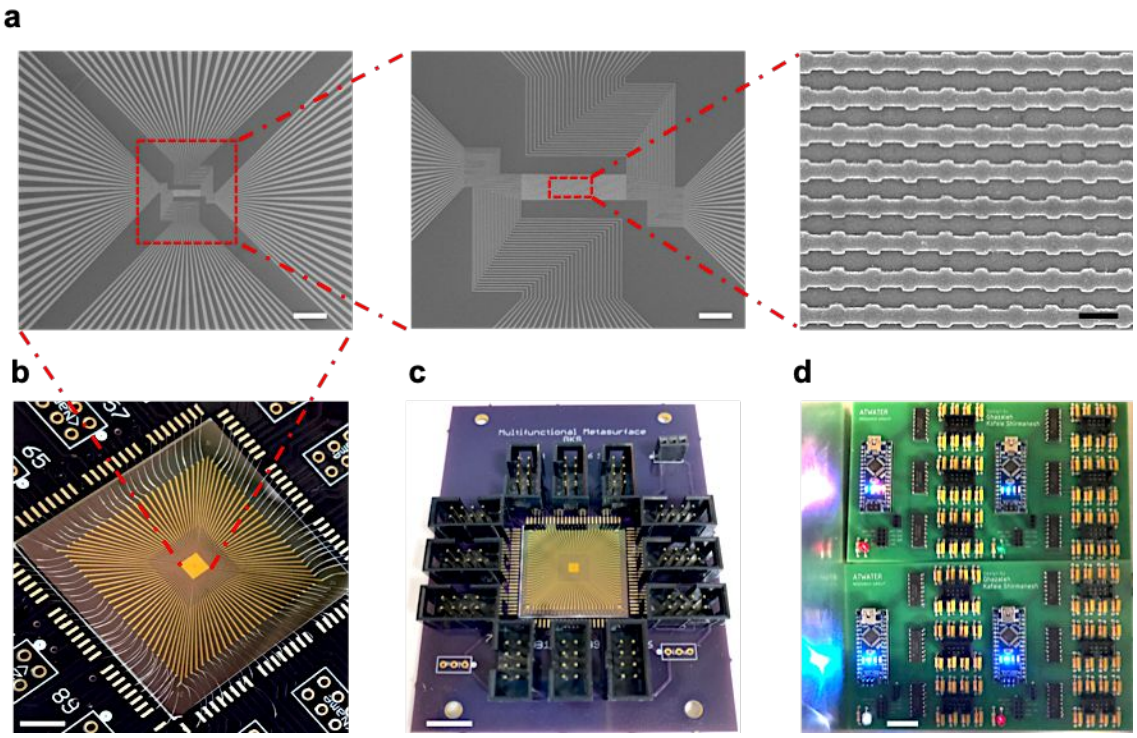

Figure 3. Fabrication and measurement of a multifunctional metasurface. (a) Scanning electron microscope image of the nanoantennas of the fabricated gate-tunable metasurface for the demonstration of dynamic beam steering and a reconfigurable focusing meta-mirror. The scale bars from left to right are 200 μm, 50 μm, and 500 nm respectively. (b) Photographic image of the multifunctional metasurface with 96 independently addressable elements. Scale bar is 5 mm. (c) Sample mounting circuit board to which we wire-bond the multifunctional metasurface pads. 96 metasurface elements' pads and 4 ITO pads are wire-bonded from the sample to 100 conducting pads on the first circuit board. Scale bar is 10 mm. (d) Voltage deriving PCB that provides 100 voltages controlled by programming micro-controllers. Scale bar is 20 mm.

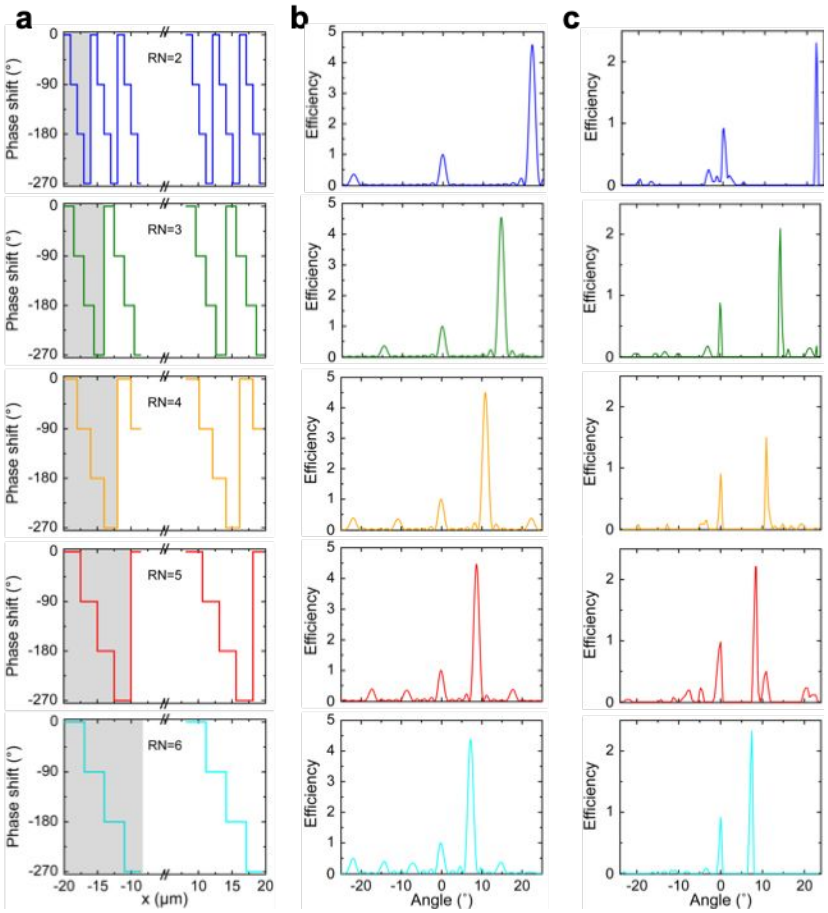

Figure 4. Demonstration of dynamic beam steering by the multifunctional metasurface. (a) The spatial phase distributions of the metasurface elements with different repeat number (*RN*) values that are used to create phase gradients resulting in beam steering. (b) Simulation results of the beam steering metasurface obtained through analytical calculations. Changing the *RN* value from 2 to 6, the steering angles of 22.17°, 14.56°, 10.86°, 8.66°, and 7.20° were obtained through calculations. (c) Experimental results of the beam steering metasurface. Changing the *RN* value from 2 to 6, we could obtain the steering angles of 22.19°, 14.43°, 10.91°, 8.51°, and 7.40°. Each steering angle corresponds to the spatial phase distribution of the same color presented in (a).

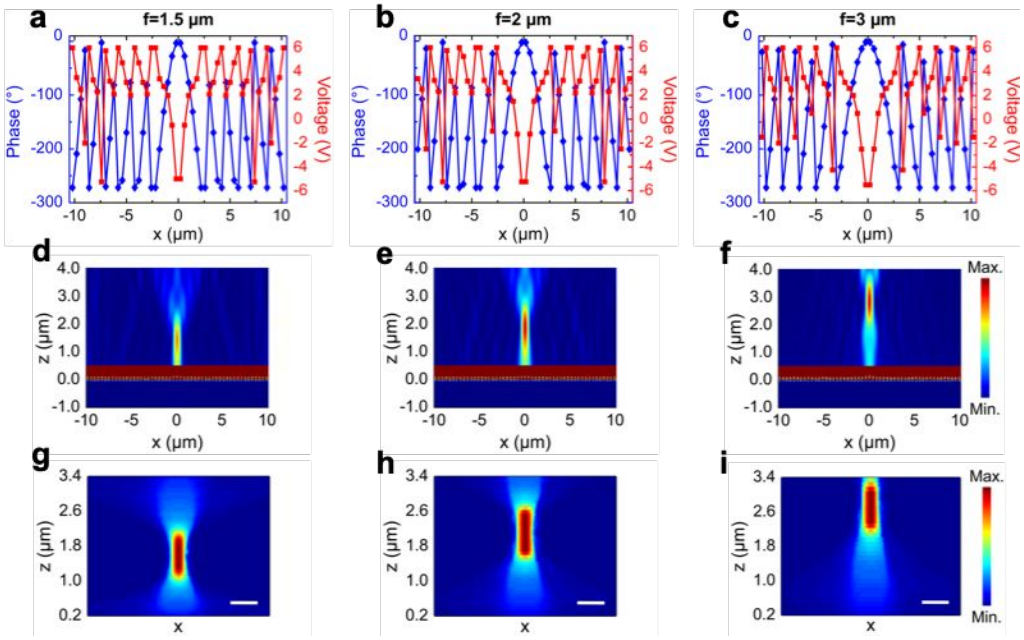

Figure 5. Demonstration of a dynamic focusing meta-mirror. Spatial phase (diamond) and voltage (square) distribution of a focusing meta-mirror with focal lengths of (a) f = 1.5 μm, (b) f = 2 μm, and (c) f = 3 μm using the phase shifts obtained from the simulation. Full-wave simulation of the spatial distribution of the electric field $|E|^2$ for the focusing meta-mirror with focal lengths of (d) f = 1.5 μm, (e) f = 2 μm, and (f) f = 3 μm. Measured intensity profile of the beam reflected from the focusing meta-mirror with focal lengths of (g) f = 1.5 μm, (h) f = 2 μm, and (i) f = 3 μm. Scale bar is 2 μm.

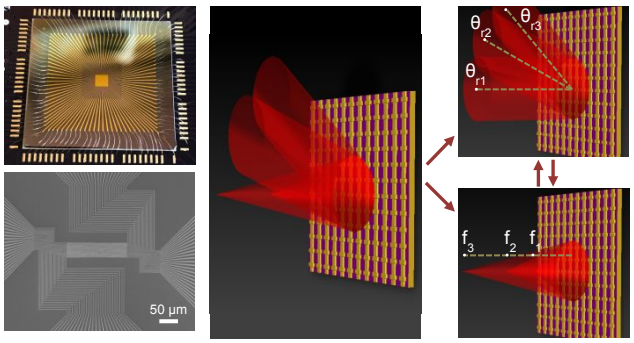

For Table of Contents Only